Enhancing the sound absorption performance of porous metals using tomography images

A.J. Otaru

Gas Turbine and Transmissions Research Centre, Faculty of Engineering, The University of Nottingham, NG7 2RD, United Kingdom

ARTICLE INFO

ABSTRACT

Commercially available porous metals are known to provide useful sound absorption, but it may be possible to modify their structures to improve their acoustical properties. Images from high-resolution X-ray computer tomography have been used to make pore-level characterization of Inconel, Recemat and Porvair foams. Based on these characterisations, flow simulations have been used to deduce parameters that determine the acoustical properties according to the Johnson-Champoux-Allard (JCA) and Delany-Bazley-Miki (DBM) models. While the DBM model enables a good agreement with measured normal incidence absorption coefficients for glass fiber materials, the JCA model enables a better agreement with data for metallic foams. The predicted sound absorption spectra were observed to depend mainly on the permeability of the porous medium being better for structures with the smallest openings and extremely poor for those with larger connectivity. It is shown that dilating the skeletal frame i.e. increasing the width of the 'struts' in a metallic foam should lead to more efficient sound absorption. It is the hope that this approach would lend itself well to use in the design of enhanced soundproofing porous metals.

© 2018 Elsevier Ltd. All rights reserved.

Acoustic foams are used to minimize reflections and reverberation, in music rooms, studios, and cinemas in a variety of locations. The use of fibrous as sound absorbing material is commercially known. Synthetic fibers like kevlar, polyester, polyurethane, melamine, polyethylene, polypropylene absorb most sound energy striking them and reflect very little [1]. These fibrous materials are made from high-temperature extrusion and industrial processes based on synthetic chemicals (petrochemical source). Their carbon footprint is quite significant, and their manufacturing processes contribute to release of some greenhouse gasses like methane, carbon dioxide, sulfur dioxide [2].

Natural fibrous materials (wool, cotton, asbestos, fur felt, hemp, flax) are generally porous and can absorb sound both at low and high frequencies [3]. They are biodegradable, inexpensive, and environmentally friendly but their low strength, softness, decrease in absorption potential over time [4] and damage to the respiratory system, human skin, eye and mucous membrane during production [5] is of concern and has limited the use of this material. Studies have shown that the broadband characteristics of noise reduction can be achieved through open-celled metallic foam structures [6,7] and have earned significant attention resulting from increased worldwide technological research and development. They are expensive to produce but are environmentally

friendly, easily recycled, high durability and resistance, less harmful, can be used to reduce vibrations and longer useful lifetimes.

Commercially available open-celled metallic foam structures (Fig. 1) such as nickel, steel, titanium, copper, and aluminium have low weight, high stiffness, an excellent fire resistance and low moisture absorption. They are generally considered as poor sound absorbers when compared to the performance of hard-backed fibrous materials especially at the region of quarter wavelength layer resonance frequencies ($\leq$2.0 kHz). The performance enhancement of these materials as described in [6–9] can be achieved through hole-drilling or rolling and prearrangement of space fillers adopting replication casting method of foam production [16]. Air gap insertion or presence of back cavity (which predominantly becomes Helmholtz resonance absorption) [10] and increased porous layer thickness are described in [11,12] to enhance the sound absorption performance of porous absorbers. An experimental study on the sound absorption coefficient measurements of Alporas foam structure in [13] pointed out the sound absorption spectra of this porous medium increases with a decrease in the relative density (R.D) of the sample. The relative density was observed to be small ($\sim$0.1) for effective sound absorption and under compression, sample porosity decreases (becoming closed-cells) and a shift in the absorption curve to the frequency minimum (or a reduction in the frequency of the quarter wavelength layer resonance) and
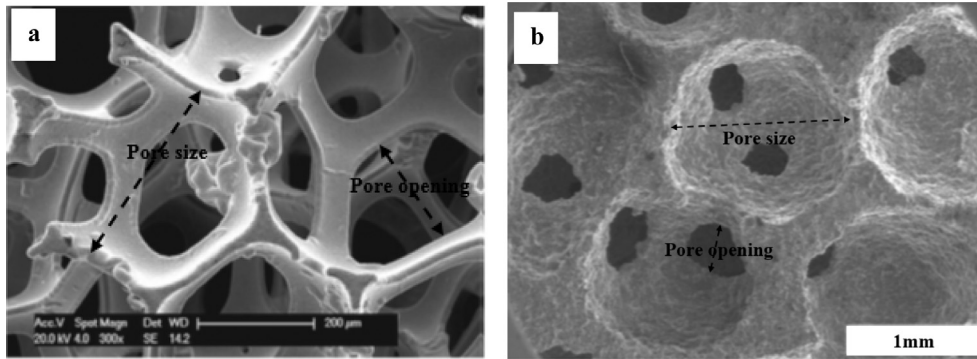
Fig. 1. Scanning electron micrographs (SEM) of (a) pure nickel 450 µm foam [15] and (b) "bottleneck-type" aluminium foam made by replication casting process [7,16] showing the typical pore sizes and openings.

reduced peak of absorption were observed when compared to a non-compressed foam of similar thickness.

A previous study reported in [16], showed that the predicted sound absorption coefficient spectra of low-density "bottleneck-type" porous structures (Fig. 1b) look better for structures with mean opening to pore size ratio ranging between 0.1 and 0.3 and permeability in the order of 10^{-10} m^2. Though, the performance of these structures were observably poor, typically, beyond the quarter wavelength layer resonance frequencies due to their low porosity, stiffness (deformation resistance) and surface area being significantly difference from those for highly porous fibrous materials. Also, the compression technique described in [13] has been successfully adopted by many researchers in this field to make useful high-density porous metals. To minimize the number of design iteration, operational cost and time, we look to explore the contribution of pore-structure related parameters of high-density porous metallic foams working from tomography images of "real" structures to describe the acoustic response of the materials and to provide some optimal values of structural information needed to design self-supporting sound absorption porous metals.

Structural characterisation of the porous structures was carried out using pore-level approach by taking a high-resolution (15 µm voxel dimension in x, y and z coordinates) X-ray computerized tomography (CT) images of the porous metallic structures. These high-density porous metals are Inconel 450 µm, Inconel 1200 µm, Recemat RCM-NCX 1116, Recemat RCM-NCX1723 and Porvair 7PPI foams. The ScanIP module of Simpleware™ (3D image processing software) was used for processing of the 2D CT images into the 3D volume. To minimize noise effect within masked structure, smart mask filtering process (with 20 iterations) was preferred over recursive Gaussian due to the important preservation of pore geometry, in particular, the pore openings of the porous materials. Unlike recursive Gaussian filtering, the ScanIP in-built smart mask filter is a smoothing algorithm that helps preserve volume and geometry of the structures [14]. The geometry preservation means that the "connecting struts" are not reduced or separated by the filtering process and volume preservation means that the important openings, cell (pore) sizes and volume of the segmented mask are not affected by the filtering process. Structural characterization was done on a representative volume that is 8–10 times the pore sizes taken from the center of the 3D structure with porosity differing by ±2 percent. Pore sizes were obtained through a watershed segmentation (disconnecting pores) of the RVE fluid domain whilst the openings were achieved by running a centreline through the pores and connectivity of the 3D RVE CT structure. Fig. 2 (top, left–right) presents the two-dimensional image of the high-resolution CT structure, three-dimensional reconstructed volume, three-dimensional representative volume

element (RVE) and an expanded view of the Inconel 450 µm foam sample. Images of the disconnected pores of the RVE microstructure are presented in Fig. 2 (mid-section) while the bottom section of the Figure represents images of the meshed structures, CFD computed velocity and pressure plots.

Up to eight parameters are used to describe the acoustical properties of porous materials [17,25] but only five parameters of the Johnson-Champoux-Allard model are determined in this work. These parameters are open porosity ($\varnothing$), airflow resistivity (σ), high-frequency tortuosity (τ), viscous characteristic length (Λ), and thermal characteristic length ($\bar{\Lambda}$). The Porosities of the materials were directly measured in ScanIP as the ratio of the RVE fluid volume to the total volume of the skeletal and fluid domains. The high-frequency tortuosity of the materials was also measured in ScanIP as the ratio of the shortest route to the sample thickness, obtained from the centre lines of RVE structural phase of the porous materials. The airflow resistivity of the materials was determined as the ratio of the dynamic viscosity of air to the permeability of the porous medium. Flow permeability of the materials were accounted for by computational fluid dynamics (CFD) modelling of the pressure drops developed across the meshed fluid domain of the porous structures in the Darcy regime using the well-known low velocity Stokes equation. Velocity inlet, zero pressure outlet, zero-velocity at the walls and symmetrical boundary conditions on the opposite side faces were imposed on the meshed matrix in the fluid module of Comsol Multiphysics 5.2™.

The choice of mesh and optimum meshing parameters were obtained through a workable mesh scale dependent study conducted using a high-density hexahedral quadratic tetrahedral meshes (HQTM) in the order of 30–40 Mcells as the basis for computation using the +FLOW solver of Simpleware™. An optimised linear tetrahedral meshes (LTM) with mesh density in the ranges of 2.0–2.5Mcells was obtained to capture the gradient of velocity within the openings of the porous materials. By plotting the CFD computed pressure drop per unit length (∇p) against superficial fluid inlet velocity and a fit into Eq. (1), the permeability of the porous structures was attained. For all the five foam structures, tolerable 4 percent less in permeability values of the HQTM based meshed structures were observed for the LTM based mesh structures. The viscous characteristic length (Λ) was determined to be twice the ratio of weighted by the velocity in the RVE volume and that of the RVE surface whilst the thermal characteristic length ($\bar{\Lambda}$) was determined to be twice the ratio of the wet pore RVE volume to the interconnected pore RVE surface as reported in [15].
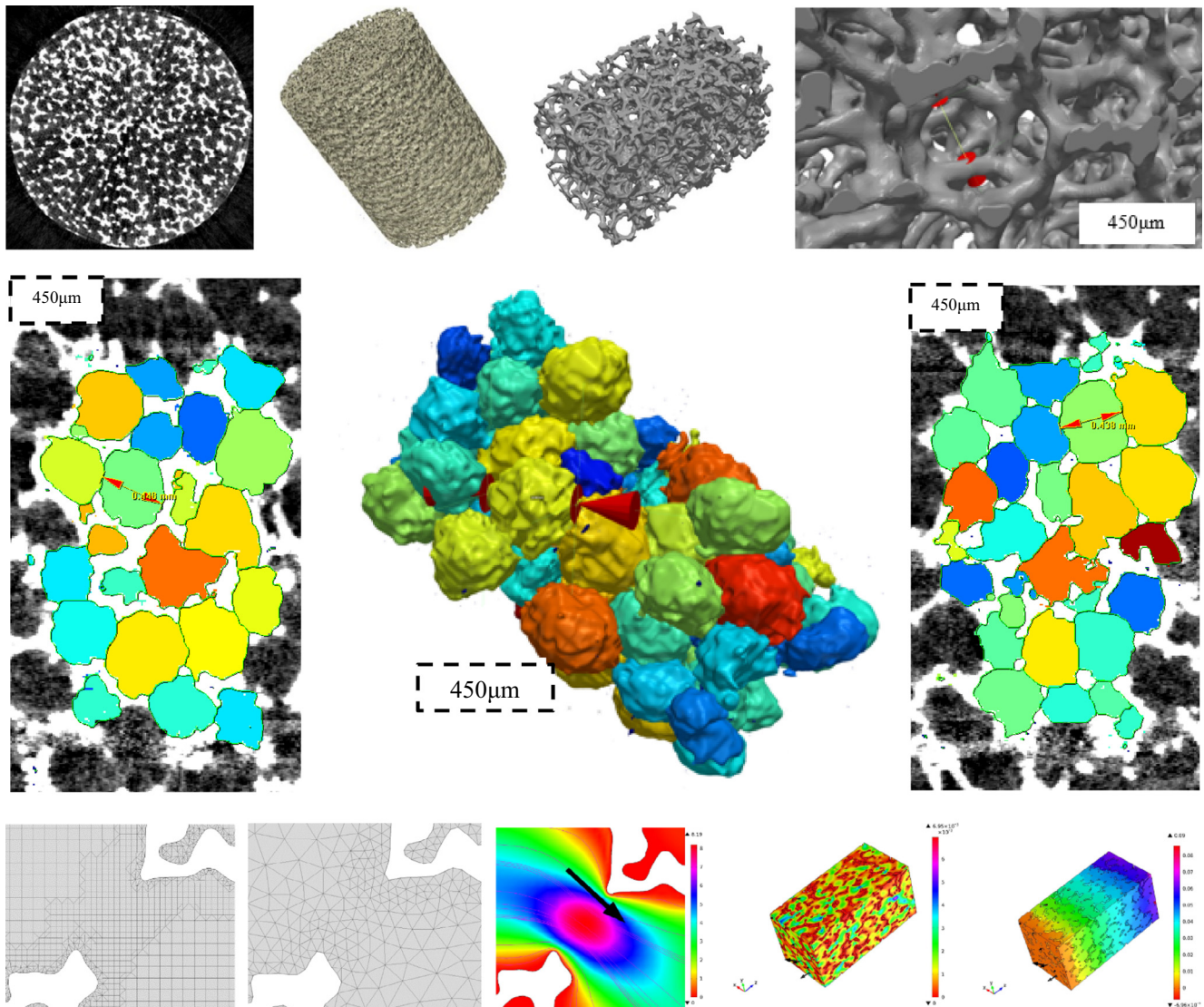
$$v_s = -\frac{k_o}{\mu} * \nabla p \qquad (1)$$

Fig. 2. Top, left-right: a 2D tomography images, 3D reconstructed volume, 3D representative volume element (RVE) and expanded view showing typical pore opening of Inconel 450 μm porous metallic structure. Images of the two (from different sections) and three-dimensional watershed segmented (disconnected pores) are represented in the mid-section. Additionally, bottom, left-right represent a 2D hexahedral quadratic tetrahedral mesh (HQTM), linear tetrahedral meshes (LTM), 2D streamline velocity plot of a "window" connecting two pores of the porous material, 3D velocity and pressure streamline plots for the Inc 450 μm porous metallic structure.

Pressure wave simulation across the porous structures was done using a similar approach presented in [16]. In brief, a 3D half-tube was created to mimic a realistic AFD 1200- AcoustiTube® 4-microphones standing wave impedance tube whose working principle is based on British standard ISO 10534-2:2001 transfer-matrix method credited to [18] and used in [10] for acoustic absorption measurements of porous aluminium structures (Fig. 3). Inbuilt air at STP was used as the material occupying the fluid domain within the tube geometry. A workable linear tetrahedral mesh (LTM) of 1.3 maximum growth rate and maximum elemental sizes half the minimum wavelength was applied to the entire domains. The Helmholtz linear acoustic frequency domain was solved on the fluid and perfectly matched layer domains whilst the poroacoustic models were resolved on the porous layer with defined pore-structure related parameters obtained using the processed computerized tomography (CT) images thereof. A background pressure field boundary condition (BC) was applied to the fluid and perfectly matched layer (PML) domains and symmetrical BC to the side walls. The inlet of the PML and the tube outlet were confined to sound hard boundary conditions. Ranges of frequencies between 100 and 6500 Hz were studied and the computational time needed to resolve a solution is also dependent on the frequency step. In this study, 100 Hz was used as frequency step and the resulting 65 frequencies were resolved within 3–4 min for each material.

The DBM model has been used to validate the numerical modelling by comparing with acoustical data for a glass wool fiber (GWF) material [3] as well as porous sintered fiber (SFM) metal [8] and nickel-chrome extra strong (NCX 2733) foam materials [20]. Tabular representations of pore-structure related parameters of these materials extracted from literature [3,8,21] and the five porous metallic structures used in this study are presented in Table 1. In the case of glass wool fiber material (GWF), an overall better fit to the experimental scatter was observed in Fig. 4 using the DBM-1 parameter (permeability) model than the JCA-5 parameters model. A likely cause of the better agreement is that the DBM (empirical) model was developed from impedance data for fibrous materials characterized by hollow struts and porosity close to
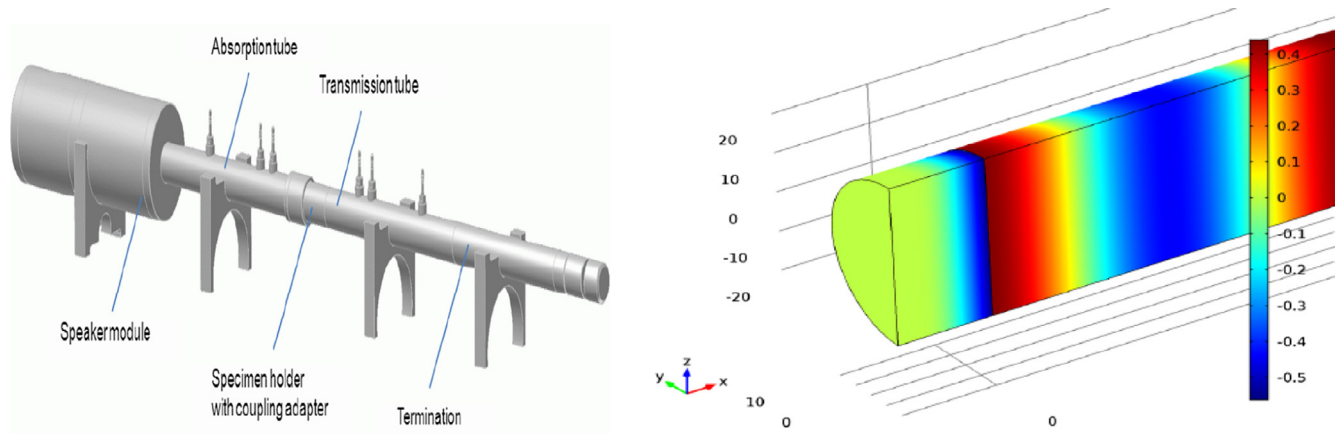
Fig. 3. Left, an AFD 1200-AcoustiTube® – measuring setup with sample holding section (adapted from AFD Analysis software 1201 user guide [20]) and right, is the 3D half-tube model representations of total acoustic pressure (Pa) computed for 25 mm hardbacked glass wool fiber computed using Johnson-Champoux-Allard model.

Table 1
A tabular representation of X-ray CT characterized pore-structure related and flow macroscopic parameters of porous metallic structures.

| Sample	Dp (mm)	Dw (mm)	σ_{FB} (mm^{-1})	σ_{FF} (mm^{-1})	$\varnothing$ (%)	τ	Λ (μm)	$\bar{\Lambda}$ (μm)	k_0 (m^2)
Inc 450 μm	0.45	0.240	8.63	43.82	83.54	1.50	133.07	390.13	1.22E−09
Inc 1200 μm	1.23	0.49	3.22	31.10	90.62	1.31	431.62	822.23	1.53E−08
RCM-NCX 1116	2.45	1.29	1.52	13.28	89.81	1.34	910.95	1773.31	6.67E−08
RCM-NCX 1723	1.86	0.69	3.01	12.80	80.96	1.52	499.64	988.55	1.62E−08
Porvair 7PPI	1.47	0.86	2.25	19.60	89.69	1.37	584.48	1269.32	2.74E−08
Inc 450 μm DL1	0.35	0.17	11.89	28.49	70.54	1.71	96.25	302.88	4.75E−10
Inc 450 μm DL2	0.29	0.12	15.37	20.80	57.50	1.88	64.43	246.80	1.57E−10
GWF	25.00 mm thick glass wool fiber material [3]				98.70	1.01	132.00	237.00	1.08E−09
SFM	23.31 mm thick porous sintered fiber metals [8]				90.94	1.51	112.99	193.78	9.59E−10
NCX 2733	10 mm thick nickel-chrome extra strong [19]				89.93	1.15	308.69	343.71	2.86E−09
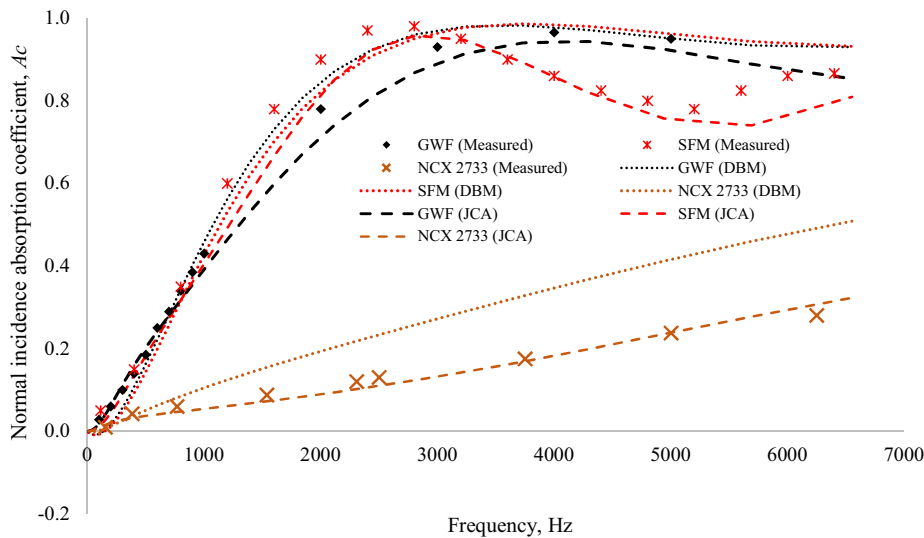
Fig. 4. Plots of measured (literature) and simulated (current) normal incidence absorption coefficient against frequency for a 25 mm hard-backed glass wool fiber material (GWF); 23.31 mm hardbacked porous sintered fiber metal (SFM) and 10 mm hard-backed nickel-chrome extra strong (NCX2733).

unity (Table 1). The sound absorption characteristics of many fibrous materials are reported in [3,18,24] to greatly depend on their pore morphology.

In the case of porous sintered fiber metal (SFM) [8] and nickel-chrome extra strong (NCX2733) [20] materials, the JCA-5 parameters model reliably predicts the behaviour characterized by the dip following the quarter wavelength layer resonance in the absorption spectrum when compared to the outcome of the DBM model. This indicates that more than a single permeability parameter is needed to predict the sound absorption spectra of porous metals. Calculated values of noise reduction coefficient (NRC), sound absorption average (SAA), the quarter wavelength layer resonance peak in absorption (Ap) and frequency (f_{max}) observed with the hard-backed porous layers (listed in Table 2) enable assessment of their relative acoustical performance.

Fig. 5 presents modelled plots of the characteristic sound absorption spectra against frequency for 20 mm hard-backed high-density porous metallic structures, and to include absorption

Table 2
Acoustic properties of the porous metallic structures.

Sample	NRC	SAA	Ap	f_{max}
Inc 450 µm	0.213	0.326	0.886	3500
Inc 1200 µm	0.068	0.100	0.380	4300
RCM-NCX 1116	0.033	0.048	0.205	4400
RCM-NCX 1723	0.061	0.094	0.382	3800
Porvair 7PPI	0.048	0.071	0.297	4400
Inc 450 µm DL1	0.297	0.455	0.999	3000
Inc 450 µm DL2	0.318	0.462	0.773	2900

spectra for glass wool fiber material (GWF). The difference in the sound absorption spectra is more likely attributed to their microstructural variations of the porous matrices, and most importantly, their mean openings and Darcian permeability. Highest absorption peak and a shift in the sound absorption curve to the frequency minima were achieved for the Inc 450 µm structure characterized by having the lowest mean openings and permeability as shown in Table 1. However, the lowest absorption peak and a shift in the sound absorption curve to the frequency maxima were achieved for the RCM-NCX 1116 sample characterized by having the highest mean pore openings and permeability value. Evidently, calculated values of the acoustic properties (NRC, SAA, and Ap) of the porous materials available in Table 2 were highest for the Inc 450 µm and lowest for the RCM-NCX 1116 sample. Aside from the Inc 450 µm foam structure, the sound absorption performances of the remaining four structures (Inc 1200 µm, RCM-NCX 1116, RCM-NCX 1723 and Porvair 7PPI) in Fig. 5 were relatively low. This was closely observed to be below the half absorption band (0.5) and well below the modelled sound absorption spectra of the

20 mm hardbacked glass wool fiber (GWF) material. This signifies the inability of the most commercially available porous metallic structures to cut down vibration significantly when presented with the source of sound waves.

Lowering the connectivity of the materials could prove useful in the design of porous metals with an optimal value of permeability range suitable for this process. Eroding the structural phases (removing pixel elements) of these materials (Fig. 6a) in ScanIP proves unsuitable for these high-density porous structures. This resulted in much wider pore openings and lost 'strut' within the materials. Dilating the skeletal frames (addition of pixel elements) of the porous matrices increases the specific surfaces and reduces the densities and the important mean pore openings as shown in Fig. 5a. This process (dilation) is likened to the application of high differential pressure in the realistic casting of metallic foams adopting the replication casting process of loosely packed beds of salt [22,23]. It is noteworthy to recall that the voxel size in all the three dimensions are equal to 15 µm.

An observable increase in the CFD computed velocity and pressure drops developed across the fluid phases of the "structurally-dilated" materials compared to the "real" and "structurally-eroded" materials were noted. However, computed pressure drops, and velocity distributions were lowest for the high-porosity "structurally-eroded" materials as shown in Fig. 6a (velocity) and Fig. 6c (pressures). Values of velocity and pressure distribution along with their scales recorded in the legend of the 2D plots are also represented in the Figs. 6a and 6b. The presence of high-velocity distribution across the openings of the structures highlights the importance of the flow dependence on the connectivity of these materials [16,23]. Flow through the high-porosity
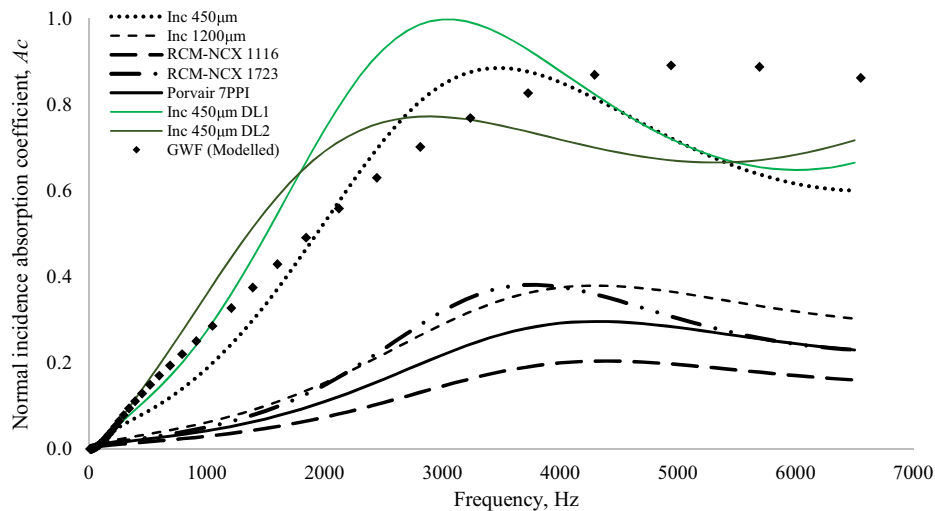

Fig 5. Plots of JCA-5 parameters simulated normal incidence absorption coefficient (Ac) against frequency (Hz) for a 20 mm-thick hardbacked Inconel 450 µm, Inconel 1200 µm, Recemat RCM-NCX 1116, Recemat RCM-1723, Porviar 7PPI, 1-pixel structurally-dilated Inconel 450 µm (DL1) and 2-pixels structurally-dilated Inconel 450 µm (DL2) structures.
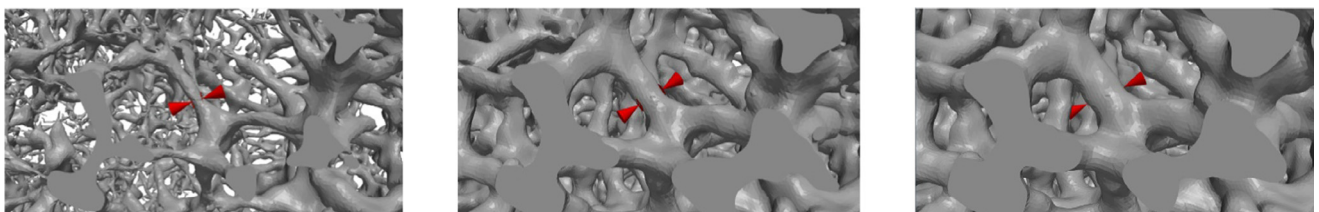

Fig. 6a. Left – right, three-dimensional eroded (1-pixel removed), real (no-erosion or dilation effect) and dilated (1-pixel added) structural phases of Inconel 450 µm porous metallic structure.
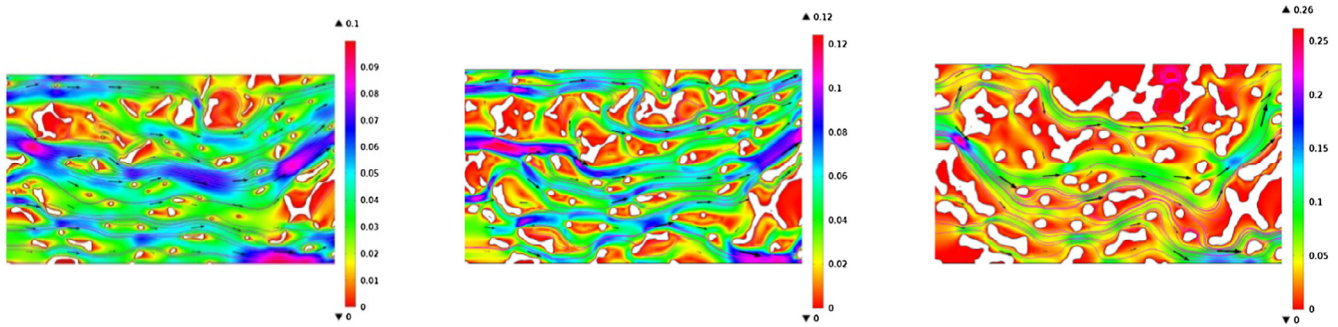
Fig. 6b. Left – right, two-dimensional velocity streamline plots for the eroded (1-pixel removed), real (no-erosion or dilation effect) and dilated (1-pixel added) structural phases of Inconel 450 μm porous metallic structure.
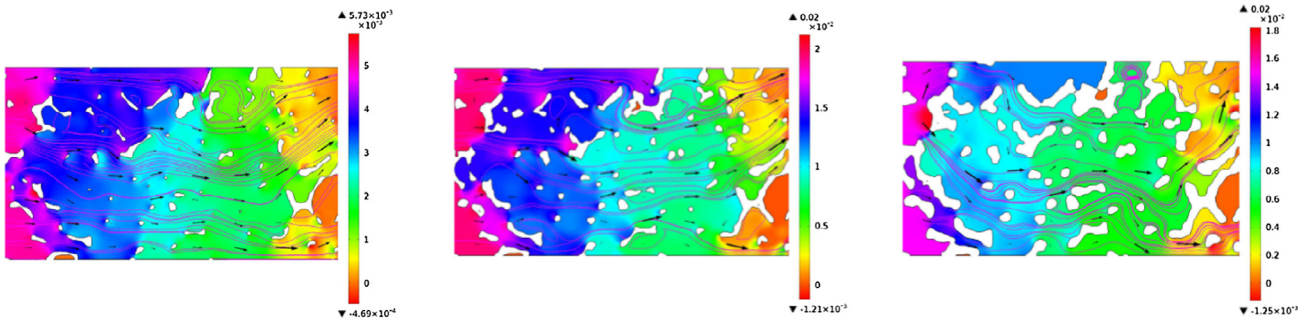

Fig. 6c. Left – right, two-dimensional pressure streamline plots for the eroded (1-pixel removed), real (no-erosion or dilation effect) and dilated (1-pixel added) structural phases of Inconel 450 μm porous metallic structure.

"structurally-eroded" materials is similar to the flow developed across a nearly-transverse isotropic medium conferred to have a low surface area with less resistance to the flowing fluid. Fluid flow developed across the "structurally-dilated" materials becomes more complicated with increased surface area and reduced porosities similar to that achieved for bottleneck-type structures reported in [16]. Additionally, changes in the flow behaviour in these materials are likely due to the changes associated with the pore-structure related parameters during these erosion-dilation processes. For instance, pore sizes and mean openings for the dilated (DL1 and DL2 for 1- and 2- pixels addition respectively) Inc 450 μm structure decrease by more than 25 per cent for each

pixel added to the frame. This, therefore, highlights the changes in the permeability of the "structurally-dilated" materials to be much lower than the obtained for the "real" Inc 450 μm sample as evidenced in Table 1.

An improvement in the acoustic properties of the adapted structures was observed for continuous dilation process; optimum for permeability between 0.5 and 1.5×10^{-09} m^2 and decrease beyond this range as showed in Fig. 7. A maximum quarter wave-length layer resonance peak in absorption (0.999) was attained for the 1-pixel "structurally-dilated" Inc 450 μm (DL1) structure in Fig. 5 and behaves extremely well at the important frequency range (200–2500 Hz) when compared to the performance of the
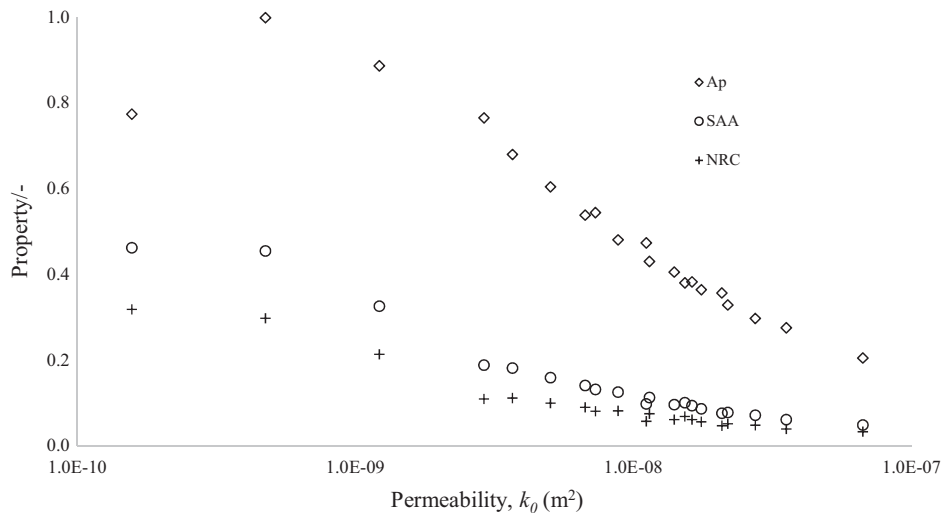

Fig. 7. Plots of simulated maximum absorption peak (*Ap*), sound absorption average (*SAA*) and noise reduction coefficient (*NRC*) against Darcian permeability (m^2) for the combined "real" and "structurally-dilated" metallic structures.

glass wool fiber material. Though, this material (GWF) performed better at the highest frequency range, typically, beyond 4750 Hz, attributable to its high porosity (Fig. 5). The characteristics absorption spectra in Fig. 5 for the "real" Inc 1200 μm porous metallic samples having the highest porosity notably has the highest absorption band and lowest for the Inc 450 μm structure characterised by having the lowest density. A further reduction in the frequency of the quarter wavelength layer resonance with much improved acoustic properties (*Ap*, *NRC* and *SAA*) were achieved by the insertion of air gap both behind (BHD) 20 mm-thick sample and between (BTW) two 10 mm optimal structures.

In conclusion, X-ray tomography images have been used to reliably characterize the pore structure-related parameters of high-density porous metallic structures used for sound absorption. In the modelling work, great care was taken to confirm the reliability and accuracy of the models, investigating the effects of the parameters selected for the models and comparing to experimental data available in the literature. The plots of the predictive characteristic sound absorption spectra of the materials were observed to depend on the pore openings and permeability of the porous medium. Structural-dilation of the skeletal frames via tomography images of these materials proves useful in the design of enhanced "semi-virtual" structures with great sound absorption potentials. It is noteworthy that for the final aspect, seeking the optimum material form to use in sound absorbing structures, it has unfortunately not been possible to manufacture and test the materials that have been designed. It is therefore advisable to recommend this for future consideration. Importantly, analytical models relating the acoustic properties and pore-structure related parameters of the porous matrices and "adapted" structures are also suggested for future consideration. This could assist in minimizing the operating cost and time arising from sound absorption measurement.

References

[1] Jorges PA, Malcom JC. Sound Vibr 2010;44:12–7.
[2] Ballagh KO. Appl Acoust 1996;48(2):101–20.
[3] Kino N, Ueno T. J App Acoust 2008;69:325.
[4] Deng XZ, Liu HS, Huang XY. Plast Sci. Tech. 2008;36(8):30–2.
[5] Ou YX. Flame retardant-manufacturing, properties & applications. Beijing: Weapon industry Press; 1997.
[6] Lu TJF, He D. J Acoust Soc Am 2000;108(4):1697–708.
[7] Li Y, Zhendong L, Han F. Procedia Mater Sci 2014;4(2014):187–90.
[8] Bo Z, Tianning C. Appl Acoust 2009;70(2009):337–46.
[9] Muhammed MM, Sa'at NA, Naim H, Isa MC, Yussof NHN, Yati MSD. Marine material research group. Malaysia: Science & Technology Research, Institute of Defence, Ministry of Defence; 2013.
[10] Han F, Seiffert G, Zhao Y, Gibbs BJ. Phys D 2003;36:294–302.
[11] Yeh JT, Yang HM, Huang SS. Poly Deg Stab 1995;50(2):229–34.
[12] Liu PS, Chen GF. Porous materials processing & applications. Tsinghua University Press Limited, Elsevier Inc.; 2014. p. 120-50.
[13] Lu TJ, Stone HA, Ashby MF. Acta Mater 1998;46:3619–35.
[14] Simpleware Reference Guide; 2014.
[15] De Carvalho TP, Morvan HP, Hargreaves DM, Oun H, Kennedy AR. Transp Porous Media 2017;117(2):311–36.
[16] Otaru AJ, Morvan HP, Kennedy AR. Scr Mater 2018;150:152–5.
[17] Dukhan N. Metal foams: fundamental & applications. DESTECH Publication, Inc. Technology & Engineering; 2013. p. 52–5.
[18] Song BH, Bolton JS. J Acoust Soc Am. 2000;107(3):1131–52.
[19] Hinze B, Rosler J. Adv Eng Mater 2014;16(3).
[20] AFD 1200 AcoustiTube® and Analysis software 1201 user guide – www.soundbook.de/download.
[21] . Dresden: Fraunhofer IFAM; 2009. 271-276.
[22] Otaru AJ, Morvan HP, Kennedy AR. Acta Mater 2018;149:265–75.
[23] Otaru AJ, Kennedy AR. Scr Mater 2016;124:30–3.
[24] Delany ME, Bazley EN. Appl Acoust 1970;3(2):105–16.
[25] Pride SR, Morgan FD, Gangi AF. Phys. Rev. B 1993;47:4964–78.